Front. Earth Sci. 2023, 17(2): 527–546
https://doi.org/10.1007/s11707-022-1002-5

RESEARCH ARTICLE

An advection fog event response to future climate forcing in the 2030s–2080s: a case study for Shanghai

Ying GU[1], Hiroyuki KUSAKA (✉)[2], Quang-Van DOAN[2]

1 School of Air Transportation, Shanghai University of Engineering Science, Shanghai 201620, China
2 Center for Computational Sciences, University of Tsukuba, 1-1-1 Tennodai, Tsukuba, Ibaraki 305-8577, Japan

Abstract Fog may continue to inhibit industry in the future. Here, we focused on a specific advection fog event in Shanghai, China, and applied a pseudo global warming method to examine advection fog under the RCP8.5 high-emission scenario. The method involved downscaling the future atmospheric conditions over the ensemble average of 19 global climate models from the fifth phase of the Coupled Model Intercomparison Project (CMIP5). We used the Weather Research and Forecasting Model coupled with a single-layer urban canopy model (WRF–UCM) to run four sensitivity experiments and examined the advection fog and its relationship to changes in meteorological conditions. The results showed that: 1) The advection fog event tended to remain in Shanghai despite global warming; 2) advection fog will not change greatly in the future; however, the onset and dissipation times will change slightly; 3) relative humidity (RH) locally increases prior to the onset of the advection fog, and decreases at the dissipating stage, despite the current and future experiments having the same RH initial and boundary conditions; 4) a small increase in surface air temperature and an increase in RH contribute to the early advection fog onset, and vice versa. Windspeed facilitates the early onset and dissipation of advection fog.

Keywords advection fog, global warming, PGW DDS, WRF-UCM, Shanghai

1 Introduction

Fog is a ground-level cloud with horizontal visibility of less than approximately 1 km. When fog occurs, it generally hinders human activities, especially transportation. Road closures due to low visibility exacerbate road congestion, reduce cargo transport efficiency, and increase transportation costs. For aviation, delays, cancellations, and closures often induce airport chaos and serious economic losses. For example, from the evening of 31 March to the morning of 1 April, 2021, more than 100 flights were canceled due to fog at Shanghai Hongqiao International Airport and Pudong International Airport. On 21–22 February, 2012, 300 flights were canceled due to fog, 440 flights were delayed, and 150 flights were diverted from Shanghai Pudong International Airport to other airports.

Global warming (GW) may affect fog by changing the local meteorological conditions. For example, an increase in radiative heating at night can warm the surface, hindering fog formation. Near-surface atmospheric stability can also be weakened and even destroyed due to an increasing in surface air temperature. These two conditions tend to reduce the occurrence of fog, especially radiation fog (Gu et al., 2019). Furthermore, fog formation depends on relative humidity (RH), which is affected by air temperature. For example, Liu et al. (2018) examined the local RH changes and the causes in the Yangtze River Delta from 1970–2010. They found an obvious descending trend due to the increase in temperature under the superposition of GW and the 'analogous heat island effect', leading to a reduction in the number of fog days. Windspeed (WS) over land, especially near-surface WS, can change due to a combination of global, regional, and local-scale factors under GW (Wu et al., 2018). A decreasing trend in WS appears to be common; however, a reversal has been found since 2010 (Zeng et al., 2019). As fog involves both mesoscale and microscale aspects that are strongly affected by location, topography, underlying characteristics, and various human activities, it remains uncertain how GW will affect urban fog in the future.

One method to address this question is dynamical downscaling (DDS) with regional climate models (RCMs). One such method was developed by Kimura and Kitoh (2007) and is referred to as pseudo global warming

Received September 30, 2022; accepted June 6, 2022

E-mail: kusaka@ccs.tsukuba.ac.jp.

dynamical downscaling (PGW DDS). This method assumes that the boundary conditions are a linear coupling of the analysis/reanalysis data (observation) and the difference component of the GW estimated by global climate models (GCMs). An advantage of PGW DDS is that downscaling using RCMs minimizes the impact of bias from GCMs (Kawase et al., 2008). Another advantage is the low computational cost. This method is useful for estimating GW effects on specific past events, weather, and regional climate (e.g., Sato et al., 2007; Kawase et al., 2008, 2009; Taniguchi and Sho, 2015; Chen et al., 2020; Dai et al., 2020). The PGW DDS method can be applied to regional and urban scales (e.g., Kusaka et al., 2012; Doan and Kusaka, 2018). Moreover, PGW DDS can effectively separate anthropogenic signals from the internal noises of climate models (Xu and Yang, 2017).

Taking Shanghai as an example, the present study examined the response of an advection fog event to a future warming atmosphere during the periods of 2030–2049, 2050–2069, and 2070–2089 relative to that in the period from 1995–2004. The future atmospheric conditions were downscaled over an ensemble average of the 19 GCMs from the fifth phase of the Coupled Model Intercomparison Project (CMIP5) (Taylor et al., 2012) by PGW DDS under the high-emission scenario RCP8.5 (i.e., with emissions producing an additional 8.5 W/m^2 by 2100) (Riahi et al., 2011). The RCP8.5 was adopted by the Fifth Assessment Report (AR5) of the Intergovernmental Panel on Climate Change (IPCC). This scenario is generated under the assumptions of high population and slow technological progress. It leads to a temperature increase of approximately 4.3°C by 2100 relative to pre-industrial temperatures. Although the target of the RCP8.5 is much higher than the 1.5°C Paris Agreement goal (i.e., "well below 2 °C above preindustrial levels and pursuing efforts to limit the temperature increase to 1.5°C above pre-industrial levels"), it is a no-climate policy baseline scenario and is considered to be one of the worst-case emissions outcomes (van Vuuren et al., 2011). Thus, the present work discusses the fog response to a future warming atmosphere under the RCP8.5 scenario.

Our objectives were to: (i) investigate the impact of GW on the occurrence of advection fog in Shanghai; and (ii) explain the physical processes of advection fog change related to GW.

Section 2 describes the data and methods. Section 3 evaluates the model performance and shows the results of fog simulation under the present and future atmospheric conditions. Discussion and conclusion are presented in Sections 4 and 5.

2 Data and methods

2.1 Model description

We used the Weather Research and Forecasting (WRF) Model (version 3.9.1.1) coupled with a single-layer urban canopy model (UCM) (Kusaka et al., 2001; Kusaka and Kimura, 2004) to run the sensitivity experiments. We used four nested domains with domain 1 center at 32.0°N, 118.0°E. The horizontal spatial resolutions of each domain were 27, 9, 3, and 1 km respectively. The grids were 164 × 164 for domain 1 and 160 × 160 for the remaining domains. The fourth domain covered most areas of Shanghai (Fig. 1), a megacity in the Yangtze River estuary on the east coast of China which is often affected by fog due to its location (Zhou and Zheng, 1987; Gu et al., 2019). The East China Sea is located to the east of Shanghai and the Yangtze River flows along the north of Shanghai; these conditions provide moisture sources to Shanghai. The large thermal contrast between sea and land (especially urban areas) also promotes the movement of moist air to the land. In winter and early spring, advection fog often occurs when the wind blows from the east and south. Preceding studies indicate a decrease in fog in the last four decades due to influences from climate warming, urban expansion, and air pollution (Zhou and Zheng, 1987; Liu et al., 2018; Gu et al., 2019; Liu et al., 2020).

The vertical grid contained 46 sigma levels from the surface to 100 hPa with 13 levels under 200 m. To reduce the uncertainty due to the selection of model configurations, the ensemble method of four experiments was used (Table 1). For microphysics, Kessler is the simplest warm rain scheme. WSM6 is a complicated cold rain scheme. For planetary boundary layer, MYNN L2.5 is a local

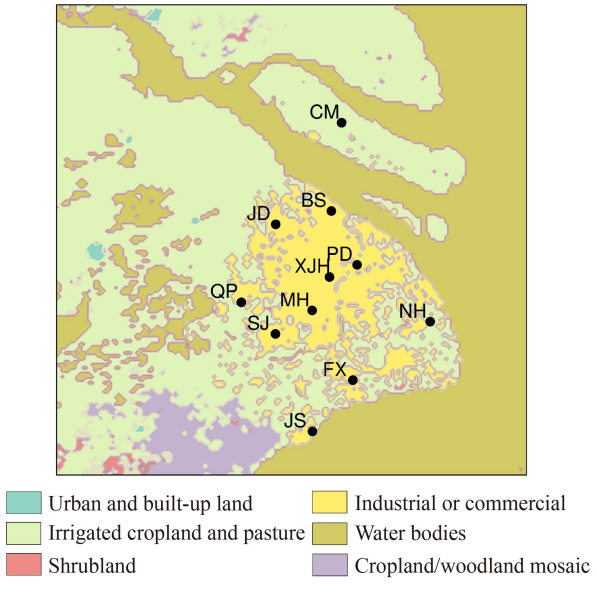

Fig. 1 Land use and land cover (LULC) setting in the fourth domain (D04) in the Weather Research and Forecasting (WRF) model and the observation sites in Shanghai. The LULC categories conform to those of the United States Geological Survey. Domain 04 covers the range from 30.57°N to 32.06°N and 120.44°E to 122.18°E. The target area (most areas of Shanghai) is from 30.67°N to 31.88°N and 120.87°E to 121.85°E.

Table 1 Four combinations of model configurations

Physical scheme	Combination 1	Combination 2	Combination 3	Combination 4
Microphysics	Kessler	WSM6	Kessler	Kessler
Longwave radiation	RRTMG	RRTMG	RRTMG	RRTM
Shortwave radiation	RRTMG	RRTMG	RRTMG	RRTM
Surface layer	MYNN L2.5	MYNN L2.5	Monin–Obukhov scheme	MYNN L2.5
Planetary boundary layer	MYNN L2.5	MYNN L2.5	YSU	MYNN L2.5
Land surface	Noah Land Surface Model			
Cumulus parameterization	Grell–Devenyi ensemble (only for D01)			

closure scheme. YSU is a non-local closure scheme. For longwave and shortwave radiation, RRTMG considers the aerosol condensational effect on clouds, whereas RRTM does not.

To run the WRF–UCM, we used 30-m LULC data from the MEGA-WEB GIS platform (Gong et al., 2017) for the year 2013 (Fig. 1), representing the current scenario. We distinguished the urban categories of commercial, high-density residential, and low-density residential. According to Gu et al. (2019), the anthropogenic heat (AH) values for each of these urban categories were approximately 96, 31, and 7 ($W \cdot m^{-2}$), respectively.

2.2 Future atmosphere data set and sensitivity experiments

The key step of PGW DDS is to estimate GW increments $\Delta\bar{V}$, hereafter GWIs (highlighted with gray rounded rectangle in Fig. A1). To obtain a GWI, we first obtained monthly-average values of the atmospheric variables from an individual GCM for both historical and future periods. The historical period, also referred to as the baseline, was 1995–2014, and the three future periods were 2030–2049, 2050–2069, and 2070–2089. Then, we calculated the ensemble mean values of the atmospheric variables over 19 CMIP5–GCMs (Table A1) for all four periods. The mean GWIs were defined as the differences between historical and a given future period. Here, we calculated GWIs for the three atmospheric variables of air temperature, geopotential height, and wind (*u*-component and *v*-component) as well as surface temperature. We used the same RH initial and boundary conditions as those in the present case (the "control experiment") for three reasons. First, the long-term global trend for land RH in the past did not change significantly (Willett et al., 2014). Secondly, RH will not change so much in the future (Takemi et al., 2012; Byrne and O'Gorman, 2016). The last reason is that we wished to evaluate how the temperature increase due to GW affects fog. For the other future boundary conditions, we added the GWIs to the historical analysis data. For more details of the role of GWI in the downscaling procedure, see Fig. A1.

Four sensitivity experiments were used. The control experiment (CTRL; bottom left in Fig. 2) was driven by the initial and boundary conditions (IBCs) derived from the National Centers for Environmental Prediction (NCEP) - final (FNL) analysis data with a horizontal grid spacing of 1°. Experiments R85–2030, R85–2050, and R85–2070 (at the bottom in Fig. 2) were forced by future atmospheric conditions estimated from the PGW DDS approach. We refer to these as the PGW experiments. These experiments were used to assess the sensitivity of fog to a warming atmosphere. To isolate and identify the impact of GW, we maintained constant LULC in all the experiments. Moreover, each experiment included four runs using four combinations of model configurations (Table 1). Then, we applied the ensemble method to obtain the results for each experiment.

2.3 Weather conditions occurring with an advection fog event

An advection fog event was observed in Shanghai from

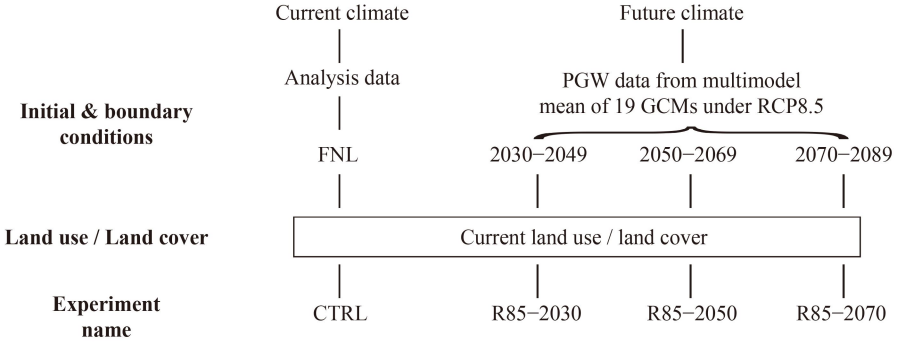

Fig. 2 Description of sensitivity experiments.

midnight on 11 February through to the morning of 12 February, 2016. At 20:00 Beijing Standard Times (BST) (12:00 UTC) on 11 February, an anticyclone north of Japan dominated the weather in most areas of the north west Pacific. Meanwhile, a cyclone developed in south-west China and an inverted trough extended eastward. At this time, the weather in Shanghai was controlled by a mean pressure field in the east part of the inverted trough. According to the sounding records at Station BS, an SE wind prevailed at the surface and an SSW wind blew at a height of 925 hPa. An isothermal layer was recorded between the heights of 1000 and 925 hPa. Mean pressure field, SE–SSW winds, and an isothermal layer are conducive to fog formation. WS in the mean pressure field is usually small. The SE–SSW winds facilitate the movement of warm and moist air into the land. An isothermal layer is stable air, which traps the moisture in the near surface.

After 23:00 BST on 11 February, fog spread out in Shanghai from the west. At 05:00 BST on 12 February, fog occurred in most areas of eastern China and southern China. At 08:00 BST on 12 February the pressure pattern was similar to that at 20:00 BST on 11 February. Under the height of 925 hPa, the wind directions (WDs) were between 145° and 180°, changing to 215° at 925 hPa. An inversion layer was observed between the heights of 993 and 964 hPa at Station BS. We developed a classification method to distinguish the types of fog (Gu et al. 2019), and the target fog case was classified as advection fog.

Here we focus on the period from 14:00 BST on 11 February to 12:00 BST on 12 February (hereafter referred to as the "study period"), which was a period covering the fog onset, development, and dissipation. Numerical experiments were run for 28 h from 08:00 BST on 11 February to 12:00 BST on 12 February, 2016, with a 6 h spin-up time. Considering the importance of lead times (Lin et al., 2017), we compared the results for 18 h and 6 h spin-up time simulations. According to Table A2, the results of the 6 h spin-up simulation were better in terms of the correlation coefficients (R) of T and RH. Hereafter, we used the 6 h spin-up time simulation results for the following discussions. Moreover, four specific times, often referred to here as "study times", are 23:00 BST on 11 February, as well as 02:00, 05:00, and 08:00 BST on 12 February.

For PGW experiments, to obtain warming signals in 2030–2049 (2050–2069/2070–2089), we calculated the GWIs between 2030 and 2049 (2050–2069/2070–2089) and the baseline. The GWIs varied between months but were identical in each year. As the runtime in the present work was from 20:00 BST on 10 February to 12:00 BST on 12 February, 2016, we calculated and added the GWI in February to FNL data and obtained the future forcing in 2030–2049 (2050–2069/2070–2089). Noticeably, the PGW method only estimated monthly-average GWIs from the simulation results of GCMs, and did not consider future changes in temporal variabilities of boundary conditions (Xu et al., 2019). In the present work, the diurnal variation in the PGW experiments remained the same as that in the CTRL. Many specific events are well-discussed, such as Sato et al. (2007), Kawase et al. (2008, 2009), Taniguchi and Sho (2015), Chen et al. (2020), and Dai et al. (2020). The present work applied the PGW method to a fog event.

2.4 Visibility algorithm

Surface visibility (VIS) is used to define fog occurrence. Fog occurs when VIS is ⩽ 1 km according to

$$\mathrm{VIS} = 1000 \times \min\left(24.135, -\ln(0.02)/\beta\right), \tag{1}$$

and

$$\mathrm{VIS} = 1609 \times 6000 \times (T - T_{\mathrm{d}})/\mathrm{RH}^{1.75}, \tag{2}$$

where VIS is surface visibility (m).

In Eq. (1), $\beta = \beta_{\mathrm{cw}} + \beta_{\mathrm{rw}} + \beta_{\mathrm{ci}} + \beta_{\mathrm{sn}}$, $\beta_{\mathrm{cw}} = 144.7 C_{\mathrm{cw}}^{0.88}$, $\beta_{\mathrm{rw}} = 2.24 C_{\mathrm{rw}}^{0.75}$, $\beta_{\mathrm{ci}} = 327.8 C_{\mathrm{ci}}^{1.00}$, $\beta_{\mathrm{sn}} = 10.36 C_{\mathrm{sn}}^{0.7776}$. C_{cw}, C_{rw}, C_{ci}, and C_{sn} are mass concentrations (g/m^3) for cloud water, rain water, cloud ice, and snow, respectively. The method is used by the NCEP Unified Post Processor V2.2. In Eq. (2), RH (%) is RH, T (°C) is the surface air temperature at 2 m; and T_{d} (°C) is the dewpoint temperature (Doran et al., 1999).

For each experiment, two visibilities were estimated using Eqs. (1) and (2). Then, the minimum of the two visibilities participated in the calculation of the ensemble mean values. If the values of two visibilities are quite different, the mean value is probably smoothed, leading to missing the fog event. Therefore, the minimum values were used.

3 Results

3.1 Model evaluation

The simulated results are from the CTRL. Figures 3–6 show the detailed time series from the 11 stations for all experiments. For T, the simulated time serials were similar to the observations. The model made an overall underestimation of T at stations NH, FX, and JS. For other stations, it underestimated T from midnight to the early morning, whereas it overestimated T from evening to nighttime and in the morning of the second day. For RH, the situation was almost the opposite. The simulations were higher than the observations from midnight to the early morning at seven stations (MH, BS, CM, XJH, PD, QP, and SJ). However, the simulated RH was lower from evening to nighttime and in the morning of the second day at these stations. The model made an overall underestimation at Station JD and an overestima-

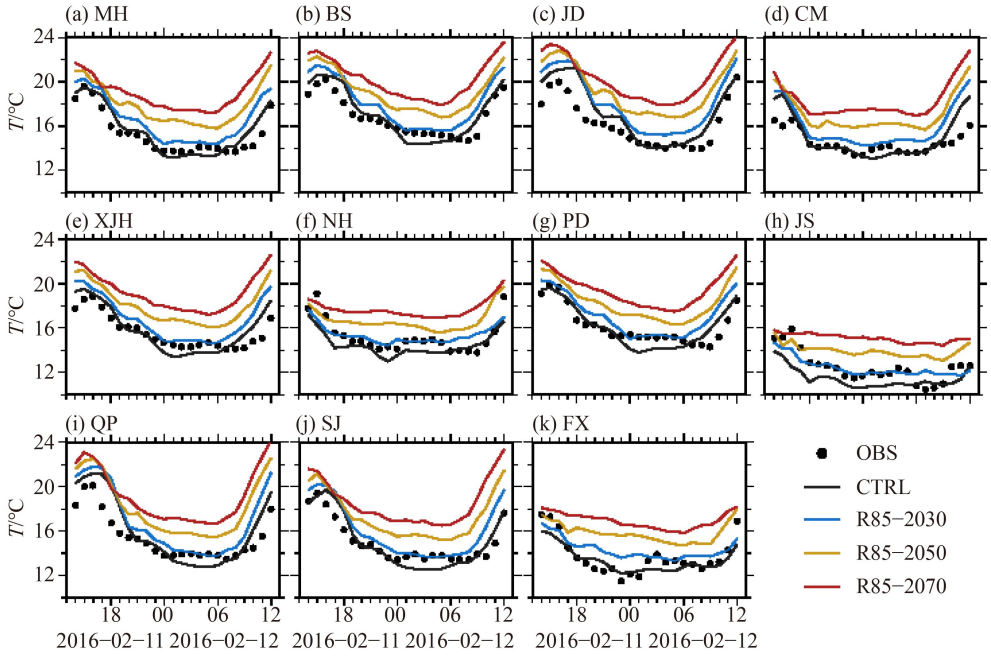

Fig. 3 Time series of the observed and simulated surface air temperature (T, °C) at each station during the fog-event study period in Shanghai. Dots represent observations. The black solid line indicates the results from the control experiment (CTRL). Blue, yellow, and red solid lines depict the results of future projections during the periods of 2030–2049 (experiment R85–2030), 2050–2069 (experiment R85–2050), and 2070–2089 (experiment R85–2070), respectively, under scenario RCP8.5.

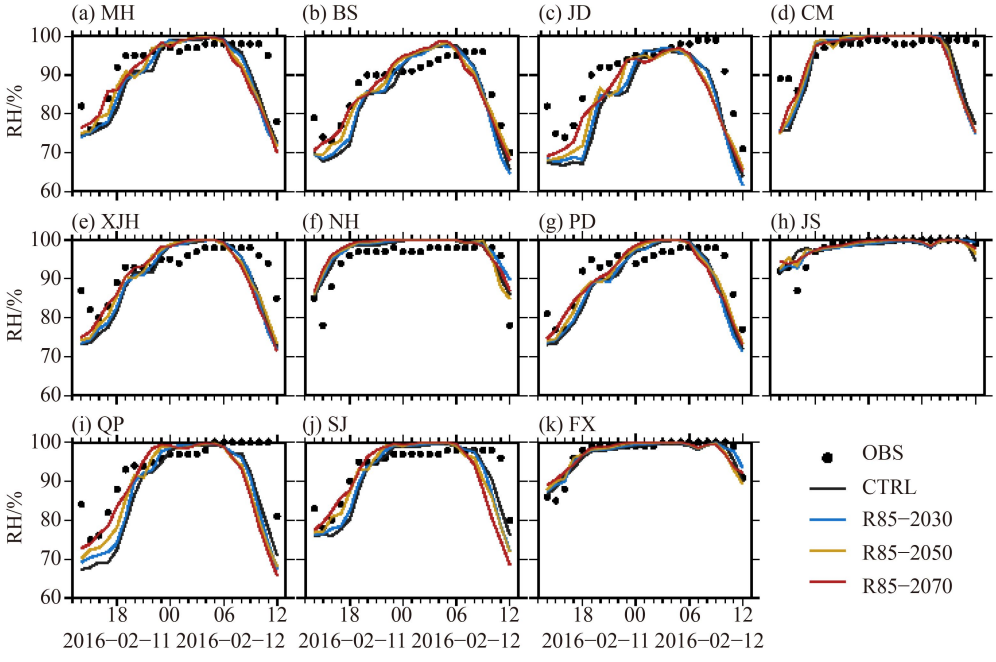

Fig. 4 Same as Fig. 3, but for relative humidity (RH, %) at 2 m.

tion at Station NH. For stations JS and FX, the simulated RH was almost the same as the observations with higher values before 18:00 BST on 11 February. For WS, the simulations were higher than the observations at all stations. For WD, the model presented the mean state but was unable to reproduce the fluctuations at some stations (e.g., MH, XJH, and CM). For VIS, the model simulated the occurrence of low visibility (< 1000 m); however, it made underestimations at nine stations (MH, CM, XJH, NH, PD, JS, QP, SJ, and FX). For Station JD, the simulations were higher than the observations. For Station BS, the model also made an underestimation of VIS from midnight to early morning; however, it did not report low visibility.

Overall, the model run of the CTRL well captured the general spatial and diurnal variations of T, RH, WD, and

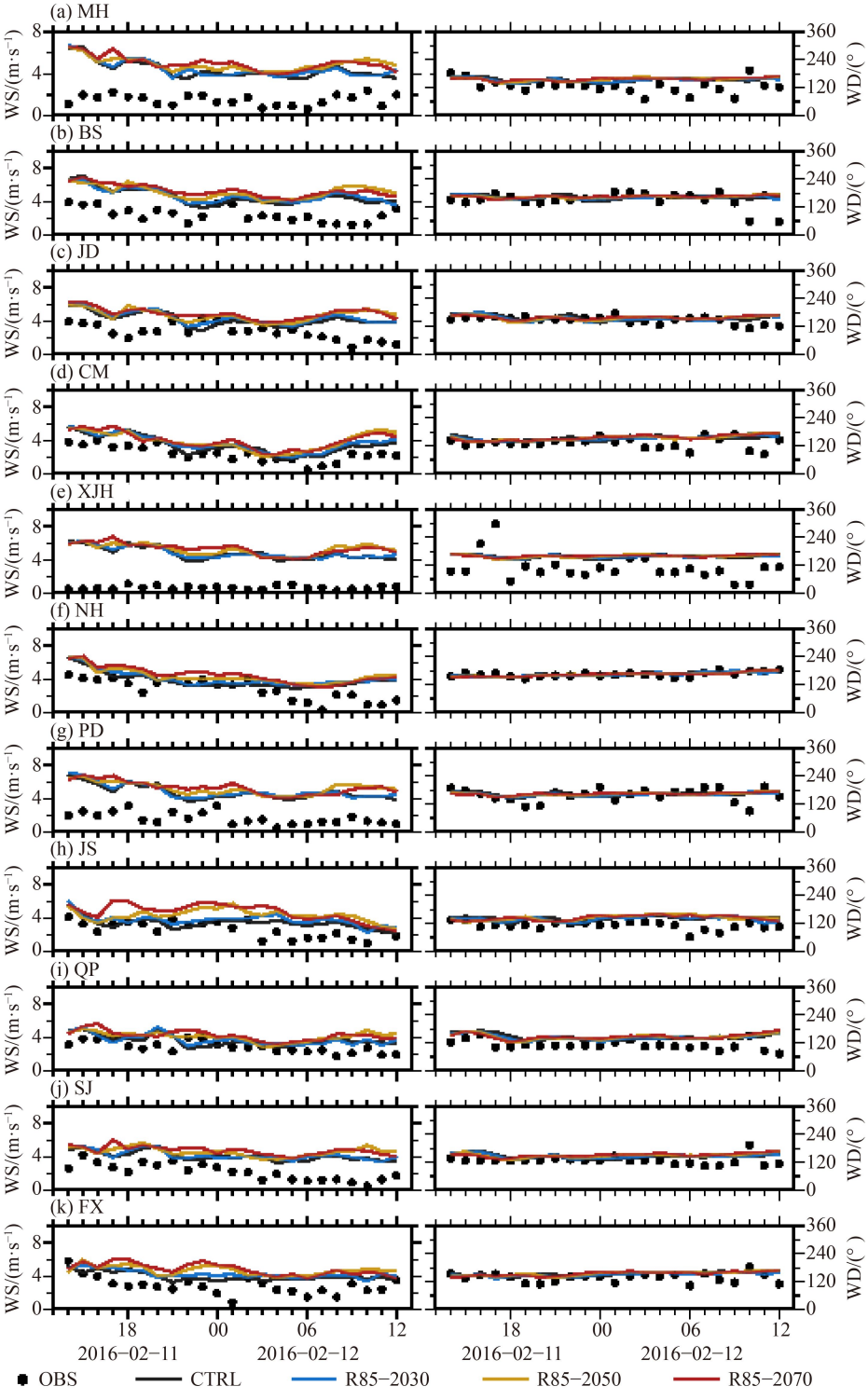

Fig. 5 Same as Fig. 3, but for windspeed (WS; m/s) and wind direction (WD; °) at 10 m.

surface VIS; however, it consistently overestimated WS. Figure A2 shows the spatial distribution of the observed and simulated meteorological variables and surface VIS at the study times. Spatially, *T* gradually increased from south to north at 23:00 BST on 11 February From 02:00 BST on 12 February, and the high *T* occurred in the north and east and decreased from the northeast to southwest. The RH was > 95% throughout most of Shanghai with relatively low areas in the north at 23:00 BST on 11 February and 08:00 BST on 12 February. Then, the VIS was < 1000 m in the south and gradually increased from south to north.

As a measure of how well the advection fog event was modeled, we calculated the *R*, bias (BIAS), and root mean

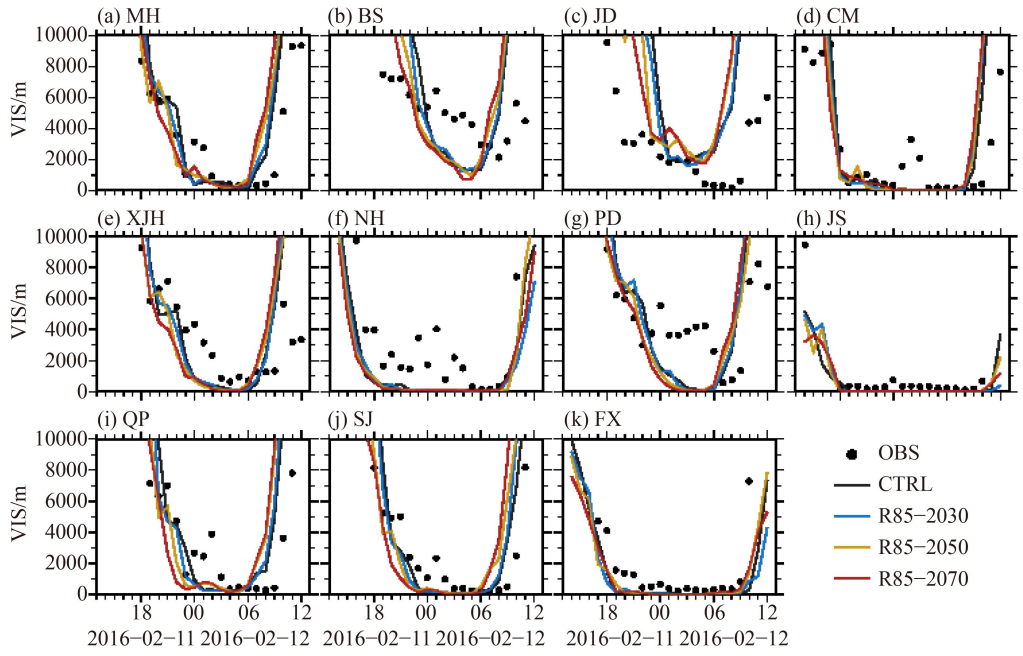

Fig. 6 Same as Fig. 3, but for visibility (VIS, m).

square errors (RMSEs) to compare the simulated results with observations. In evaluating the model's performance in terms of T, we found $R > 0.82$ at a 0.001 significance level at all stations (Table 2). BIAS at all stations was between −1.0°C and 1.0°C, and RMSEs at all stations were < 1.5°C. Thus, the model simulated T overall.

Table 2 also shows the performance results for RH and WS. For RH, the R exceed 0.64 at a 0.001 significance level at all stations. Except for stations CM and JS, the R were > 0.84. RH was underestimated, with BIAS between −7.5 and 0%. RMSEs at all stations were between 1.6 and 9.2%.

For WS, the R at stations CM, SJ, and FX exceeded 0.63 at a 0.002 significance level. WS was not well-simulated at other stations, with $R < 0.5$. The model overestimated WS at all stations, with BIAS and RMSEs of > 0.8 and 1.2, respectively.

For surface VIS, the R were > 0.71 at a 0.001 significance level at all stations. VIS was overestimated at all stations except NH, JS, and FX. BIAS was between 1574 and 6604 m. RMSEs were between 3304 and 8080 m. VIS was estimated using Eqs. (1) and (2).

The differences between simulations and observations were most likely caused by model configurations, although we used four combinations. Besides, a high estimation of anthropogenic heat is likely to results in an overestimation of T, leading to an underestimation of RH. The unsatisfying simulated WS was most likely caused

Table 2 Correlation coefficients (R), biases (BIAS), and root mean square errors (RMSEs) of the observed and simulated surface air temperatures (T, °C), relative humidity (RH, %), windspeed (WS, m/s), and surface visibility (VIS, m) for the advection fog case

Station name	T			RH			WS			VIS		
	R	BIAS/°C	RMSE/°C	R	BIAS/%	RMSE/%	R	BIAS/ (m·s^{-1})	RMSE/ (m·s^{-1})	R	BIAS/m	RMSE/ m
MH	0.94	0.3	0.8	0.84	−3.5	6.2	0.22	2.9	3.0	0.92	2044	3759
BS	0.95	0.3	0.9	0.93	−3.1	5.5	0.49	2.2	2.4	0.76	3650	6347
JD	0.94	1.0	1.4	0.90	−7.5	9.2	0.17	1.5	1.9	0.79	6604	8080
CM	0.90	0.5	1.2	0.69	−2.6	7.1	0.84	1.1	1.2	0.86	1727	4360
XJH	0.91	0.2	0.9	0.86	−3.3	6.6	−0.09	4.1	4.2	0.77	2185	5274
NH	0.86	−0.7	1.1	0.86	2.2	3.9	0.48	1.1	1.6	0.85	−2395	3668
PD	0.89	0.0	0.9	0.89	−2.9	5.3	0.40	3.1	3.2	0.83	1531	4586
JS	0.82	−1.0	1.3	0.64	0	2.6	0.43	0.8	1.2	0.71	−2643	5139
QP	0.94	0.6	1.5	0.84	−6.1	9.2	0.16	0.8	1.2	0.91	2423	4494
SJ	0.95	0	0.9	0.90	−2.1	4.8	0.65	1.9	2.0	0.95	1574	3304
FX	0.91	−0.3	0.9	0.95	−0.4	1.6	0.63	1.1	1.4	0.90	−3339	5956

by the building-related parameter settings in UCM. For VIS, the errors not only came from the model configurations but were also caused by the empirical visibility algorithms.

3.2 Changes in advection fog occurrence under RCP8.5

Under the increasing warming scenario of RCP8.5, the surface VIS will tend to decrease slightly before onset (Fig. 7). At 23:00 BST on 11 February, the VIS in most parts of northern Shanghai decreases to < 5000 m. The advection fog area then expands from south to north. At 02:00 BST the following morning, fog spreads to over half of Shanghai and continues until 05:00 BST. With the temperature increases later in the morning, the surface VIS increases to 1000 m in northern Shanghai. As a result, the advection fog dissipates.

Time series of the observed and simulated advection fog occurrence are depicted in Fig. 8. The results show that the CTRL experiment generally reproduced the advection fog well. The model overestimated the fog at seven stations (XJH, NH, PD, JS, QP, SJ, and FX) and underestimated it at two stations (JD and CM). Station BS had no fog, in agreement with the model. The simulated duration at Station MH was the same as the observation. However, the model failed to simulate the fog occurrence at Station JD.

Here we examined the fog response to future warming atmosphere by comparing CTRL and PGW experiments. We defined the onset and dissipation as the first and last fog occurrence, respectively, with the intervening time being the duration. Figure 8 shows that all 10 stations that currently experience advection fog will continue to have fog under RCP8.5, and that fog will develop at Station BS.

From 2030–2049, seven stations (MH, BS, JD, CM, XJH, PD, and QP) will tend to maintain the current situation. Station NH will experience fog dissipation that occurs 1 h later. Fog onset and dissipation will be delayed by 1 h at Station JS. However, Station SJ showed the opposite result. Fog onset at Station FX will occur 1 h earlier. In 2050–2069, the current situation will be maintained at stations MH and JD. Fog may occur at Station BS for 1 h, and will appear 1 h earlier at four stations (CM, PD, QP, and SJ). Only Station JS tends to have fog onset occurring 1 h later. Three stations (XJH, SJ, and FX) will experience fog dissipation 1 h earlier. In 2070–2089, five stations (JD, NH, JS, SJ, and FX) will have the same situation as that in 2050–2069. Station CM will experience the same fog period as that in 2030–2049. Fog will occur 1 h earlier at three stations (MH, BS, and XJH) and 2 h earlier at two stations (PD and QP). Fog will dissipate 1 h earlier at Station XJH.

Concerning fog duration, four stations (BS, NH, PD, and QP) will tend to have slight increases from 2050 to 2069 and 2070–2089 relative to the current (observed) fog duration. However, fog duration in three stations (JS, SJ, and FX) will decrease slightly. The other four stations (MH, JD, CM, and XJH) will almost maintain the current situation.

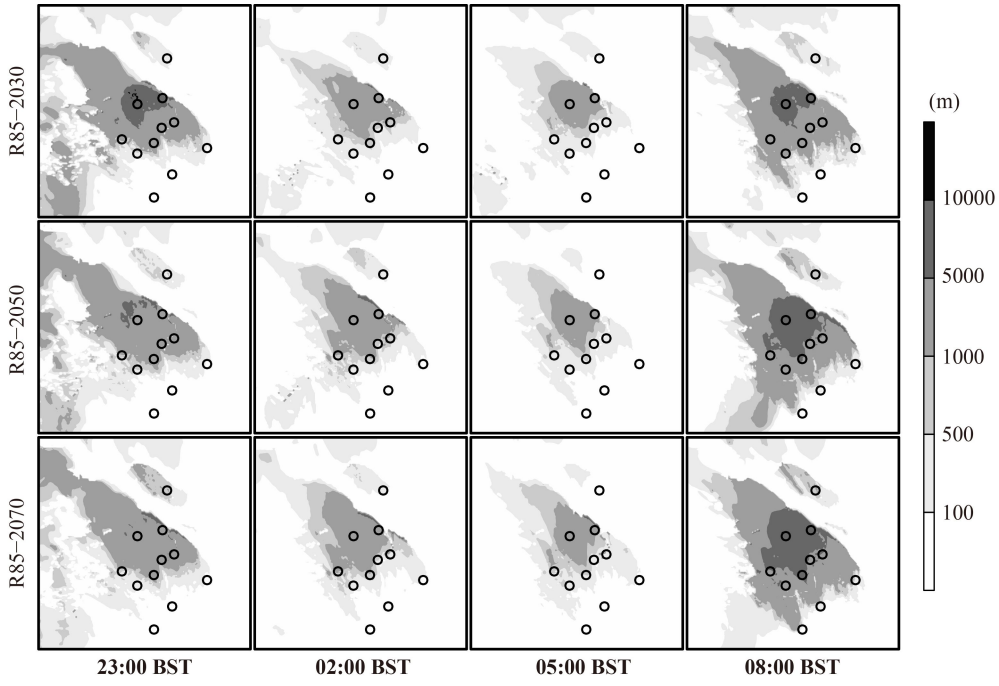

Fig. 7 Spatial distribution of surface visibility for the advection fog event at four study times during the periods of 2030–2049 (experiment R85–2030), 2050–2069 (experiment R85–2050), and 2070–2089 (experiment R85–2070) under scenario RCP8.5. The circles are observation stations in Shanghai.

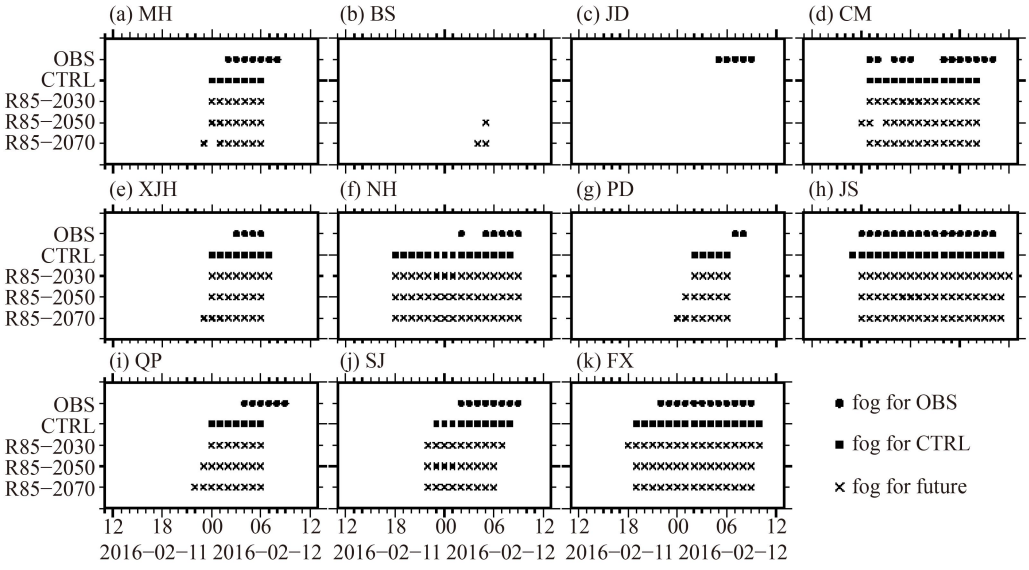

Fig. 8 Time series of the observed and simulated advection fog at 11 stations during the study period. Dots are observed cases, squares are from the control experiment (CTRL), and crosses are future projections during the periods of 2030–2049, 2050–2069, and 2070–2089 under scenario RCP8.5.

3.3 Responses of meteorological conditions under RCP8.5

3.3.1 Surface air temperature

Here we examine the future increase of T at 2 m over Shanghai. Figure 9 shows the spatial distributions of differences in T between each future projection and the CTRL during the four study times. T steadily increases in most areas of Shanghai. Typical values are 0.5°C–1.5°C by 2050, 1.5°C–3.5°C by 2070, and 3°C–4.5°C by 2090 from 23:00 on 11 February to 05:00 BST on 12 February. The average temperature also increases later in the morning, reaching 1°C at 08:00 BST from 2030 to 2049. At this time of day, the average increases are 2.3°C by 2070 and 3.8°C by 2090. By 2050, the average temperature over the 11 stations will have increased by 0.9°C–1.2°C (top row, Fig. 9); this average increase will be 2.3°C–3.0°C by 2070 (middle row; Fig. 9) and 3.5°C–4.0°C by 2090 (bottom row; Fig. 9).

Considering the temperature change during the day at each station, as shown in Fig. A3, the temperature increases almost until midnight. Then, it decreases at all stations until the early morning. Subsequently, T at two stations (QP and SJ) rapidly increases again and then decreases. Other stations exhibit a slight increase and then decrease in T.

3.3.2 Relative humidity

As for T, we examined the change of RH from that of the CTRL. In Fig. 10, we show the spatial distributions at the four study times. At 23:00 BST, RH increases in some areas in the north and west by 2050. RH continues to increase in most areas of Shanghai by 1%, with some areas in the north and west increasing by > 4% in 2050–2089. At 02:00 BST, the RH increase is less. RH in some areas in the north and west decreases by 2070 and 2090. Then, at 05:00 BST, RH is unchanged throughout Shanghai except for in a small area in the north and west that continues to have a small RH increase. At 08:00 BST, RH decreases over most areas in Shanghai, especially in the north and west, with some decreases exceeding 2% by 2070 and 3% by 2090. However, in the east, an RH decrease is not obvious and there even an increase in a small area.

The time series of RH changes at each station showed a similar trend (Fig. A4). Seven stations (MH, BS, JD, XJH, PD, QP, and SJ) will experience an obvious increase in RH before 00:00 BST on 12 February. Except for JD, the stations almost maintain the current situation until 06:00 BST on 12 February. For Station JD, RH has almost no change by 2050, and obvious decreases by 2070 and 2090 until 06:00 BST on 12 February. Subsequently, RH will initially decrease and then increase again. Station CM has a similar trend with almost no significant change from 18:00 BST on 11 February to 07:00 BST on 12 February. Compared with the above stations, three stations (NH, JS, and FX) will have a relatively small change. Station JS will experience a decrease before 18:00 BST on 11 February, and then increase to approximately zero until 10:00 BST on 12 February. Averaging the 11 stations, the RH changes are −0.4%–0.9% by 2050, −1.6%–2.1% by 2070, and −2.1%–2.4% by 2090 (Fig. 10). Negative values occur at 08:00 BST on 12 February in the three PGW experiments.

Figure 10 indicates a future change in RH, although we assumed the same RH in the initial and boundary

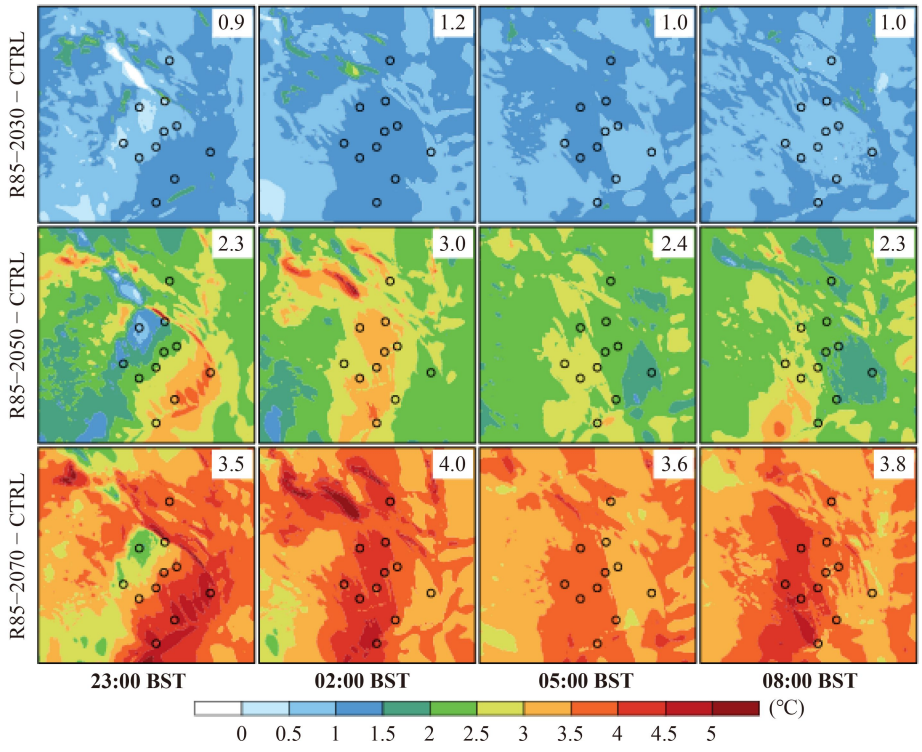

Fig. 9 Spatial distribution of differences in surface air temperature at 2 m between each future projection period and the control experiment (CTRL) for the fog event at the four study times. The circles are observation stations in Shanghai. The averages over all 11 stations are shown in the upper right in each plot.

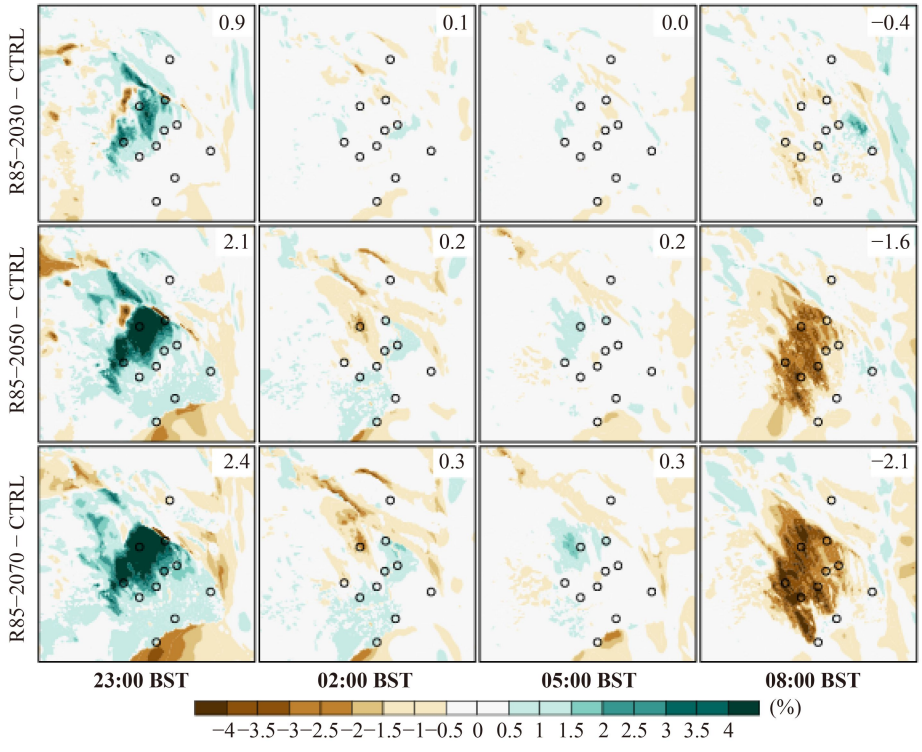

Fig. 10 Same as Fig. 9, but for relative humidity at 2 m.

conditions in both the current and PGW experiments. The mesoscale and microscale physical processes that changed the RH locally should be relevant to the future trends in the occurrence of advection fog.

3.3.3 Windspeed

As shown in Fig. 11, the future projections showed increases in WS in most areas of Shanghai. At 23:00 BST, the WS increases are 0–0.5 m/s by 2050, 0.5–1.5 m/s by 2070, and 1.5–2 m/s by 2090. WS in a small area will increase by > 2 m/s by 2090. At 02:00, 05:00, and 08:00 BST, the typical WS increases are 0–1 m/s, with a small area decreasing by −0.5–0 m/s. Figure A5 corresponds well with Fig. 11. At most stations, the WS change is positive overall. Averaging all 11 stations, the WS changes are 0.1–0.3 m/s by 2050, 0.3–1.1 m/s by 2070, and 0.5–1.6 m/s by 2090 (Fig. 11).

3.4 Potential causes of changes in advection fog occurrence

The key process of any type of fog is the conversion from water vapor to liquid water. We further examined the water vapor mixing ratio at 2 m (Q2) and cloud water mixing ratio near the surface (QC). Figure 12 demonstrates the spatial distribution of the differences in Q2 between each future projection and the CTRL. The changes of Q2 are relatively consistent; in all three PGW experiments, Q2 increases at each stage of advection fog development. The Q2 increases are < 1 g/kg by 2050, 1–2.5 g/kg by 2070, and > 2.25 g/kg by 2090 in most areas of Shanghai. The time series in Fig. A6 show that experiment R85–2070 had the highest Q2 values, and experiment R85–2030 had the lowest. This finding is consistent with the mean values of all 11 stations (Fig. 12).

Moreover, QC appears to increase in the north and west of Shanghai, while some areas in the south and east decrease at 23:00 BST on 11 February (Fig. 13). At 02:00 and 05:00 BST on 12 February, the south and east of Shanghai have an increase in QC by 2050. Most areas of Shanghai will experience decreases in QC by 2070 and 2090. At 08:00 BST on 12 February, QC will have an obvious decline in the southwest, with the maximum exceeding 0.2 g/kg.

According to Fig. 8, the target advection fog will not change greatly in the PGW experiments; however, slight changes will occur in the fog onset, dissipation, and duration times. The potential reasons for the changes are as follows.

At the fog onset stage, a large increase in T indicates that the air can hold more water vapor, and then the conversion of condensation will be inhibited, causing an increase in Q2 and a decreare in QC. As a result, RH decreases and leads to the late onset of fog at two stations (JS and FX) in coastal southern Shanghai. Conversely, a small increase in T tends to cause a small increase in Q2. Moreover, the increase in WS will bring more moisture inland. As a result, QC and RH will increase. Two inland stations (QP and SJ) in western Shanghai are likely to experience early fog onset.

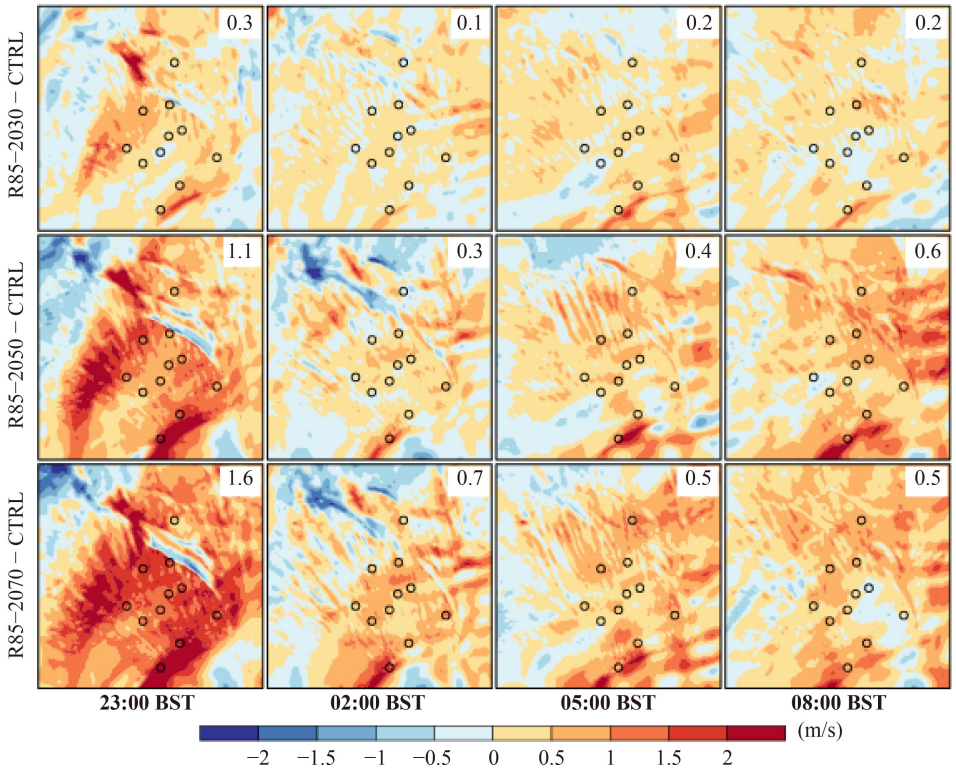

Fig. 11 Same as Fig. 9, but for windspeed at 10 m.

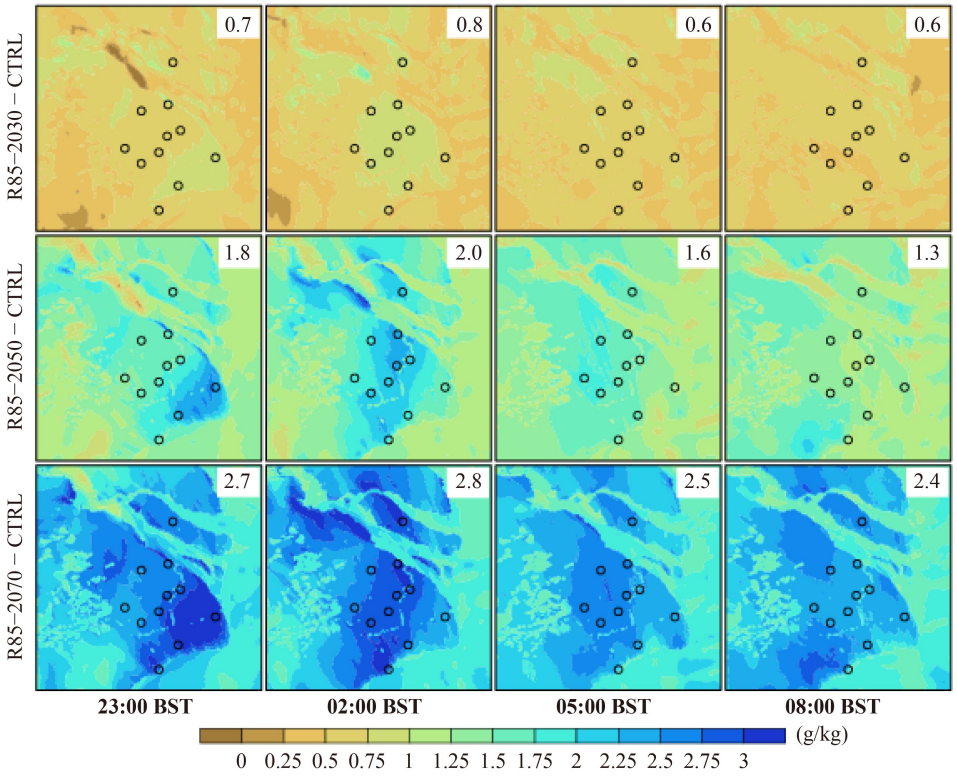

Fig. 12 Same as Fig. 9, but for water-vapor mixing ratio at 2 m.

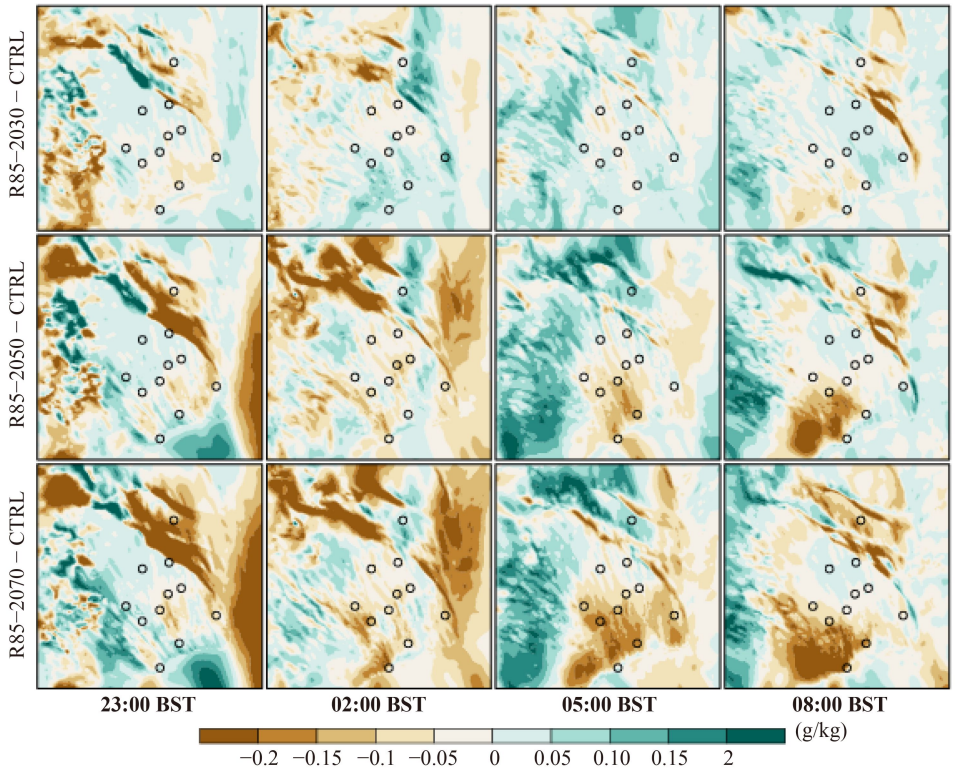

Fig. 13 Same as Fig. 9, but for cloud water mixing ratio at first model level.

Regarding the dissipating stage, early dissipation will occur with a large increase in T and a decrease in RH at some stations (e.g., SJ). Station NH in eastern Shanghai showed the opposite result. In addition, fog will dissipate early due to the WS increase at some stations (two inland stations [XJH and SJ] and a coastal southern site [FX]).

4 Discussion

In this study, we used PGW DDS to examine how an advection fog in an urban area may respond to future atmospheric warming. The higher air temperatures in the future predicted in global climate models are unfavorable to fog formation due to low RH (Liu et al., 2018). Niu et al. (2020) argued that RH should decrease more rapidly under the RCP8.5 scenario than under the RCP4.5 scenario because of the asymmetrical increase in vapor pressure and saturation vapor pressure with increasing temperature. However, our results suggest a slight change in the occurrence of advection fog under the background of GW. In the present study, RH of all experiments (current and future) was assumed to have the same initial and boundary conditions. In other words, for the large-scale atmospheric state, we assumed no change in RH. However, due to mesoscale and microscale physical processes in the experiments, the increase in moisture likely promotes the increase in local RH prior to the advection fog onset. In contrast, Niu et al. (2020) investigated the long-term trend in RH based on monthly mean values. Our results instead focused on an advection fog event. Another reason for our different findings regarding RH may involve the type of fog. The key process of radiation fog is radiative cooling, relating to temperature. The fog event here was advection fog, and thus was controlled by vertical mixing of moist air parcels with different temperatures. Therefore, under certain weather conditions, RH would increase with moisture. Our results indicate the possibility of advection fog occurrence being maintained and increasing in the future, which suggests that more research on fog trends may be useful.

Some studies have reported increasing amounts of fog, despite GW, based on long-term observations (Niu et al., 2010; Syed et al., 2012). Various suggested reasons included changes in the weakened Asia winter monsoon, increased regional aerosols sediments, and the North Atlantic Oscillation (Niu et al., 2010; Syed et al., 2012). Our results support those of these previous studies, except that our results apply to local climate change under the background of GW.

Moreover, the present work focused on the impact of GW on fog formation. We did not consider the potential influence of future urbanization in the PGW experiments. As previous studies showed, urbanization is also crucial in fog formation (Belorid et al., 2015; Williams et al., 2015). Gu et al. (2019) examined the impact of urban expansion on fog in 1989–2017. The results indicated that advection fog tends to decrease due to the increased water–vapor mixing ratio, decreased liquid water, and weakened inversion layer caused by the higher surface air temperature. As mentioned in Section 2.1, Shanghai is a global mega-city, and urban expansion will most likely continue. Figure A7 shows the prediction of LULC in the 2030s (Gong et al., 2017), which indicates that most areas of Shanghai will be urbanized by 2030. If the future emission rate of anthropogenic heat in a unit urban area maintains the current situation, anthropogenic heat will increase. Thus, the air temperature increase will continue. If the warming effect caused by urbanization is greater than that of GW, advection fog is likely to decrease in the future. However, if it is the opposite, advection fog may be maintained or increase slightly in the future. This is a subject for future study.

5 Conclusions

We evaluated the possible response of an advection fog event from the 11–12 February, 2016 in Shanghai to future atmospheric warming in three periods during 2030–2089 under RCP8.5. We used the WRF–UCM model and ran four sensitivity experiments (CTRL, R85–2030, R85–2050, and R85–2070) to examine the change in fog occurrence and its relationships to changes in meteorological conditions. We used the PGW DDS method to create a future warming atmosphere. Our main results are summarized as follows.

1) Shanghai's future climate due to the warming atmosphere is likely to continue to have advection fog.

2) Advection fog will not change greatly in the future; however, the onset and dissipation time will change slightly.

3) T will increase by 0.9°C–1.0°C in 2030–2049, by 2.3°C–3.0°C in 2050–2069, and by 3.5°C–4.0°C in 2070–2089. RH will increase before fog onset and decrease at the dissipating stage. WS will also tend to increase by 0.1–0.3 m/s in 2030–2049, by 0.3–1.1 m/s in 2050–2069, and 0.5–1.6 m/s in 2070–2089.

4) A small increase in T and increase in RH contribute to early advection fog onset and vice versa, and WS facilitates early onset and dissipation.

Acknowledgments This work was supported by the National Natural Science Foundation of China (Grant No. 52175103). We would like to thank Lidia Lazarova Vitanova from Nikken Sekkei Research Institute, Tokyo, Japan for assistance in postprocessing of the simulations.

Appendix A

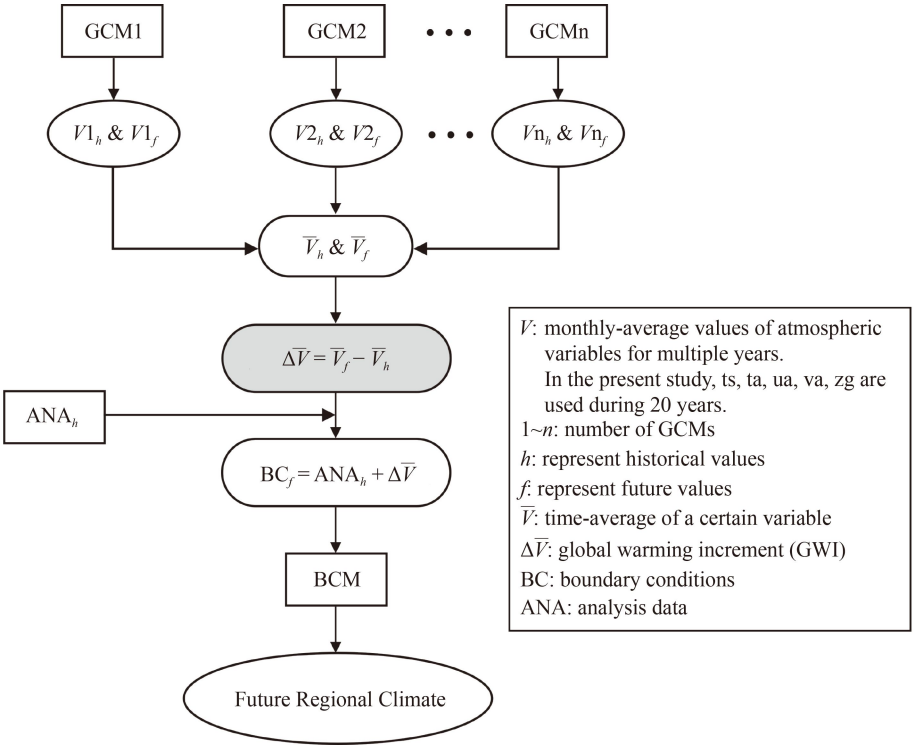

Fig. A1 Flowchart of pseudo global warming dynamical downscaling (PGW DDS). The gray rounded rectangle shows the calculation of global warming increments (GWIs) ($\Delta\overline{V}$).

Table A1 Overview of the 19 CMIP5 global climate models (GCMs) used in this study

No.	Model name	Institute (country)	Resolution (lon. × lat.)
1	ACCESS1.0	Commonwealth Scientific and Industrial Research Organisation (CSIRO) and Bureau of Meteorology (BoM) (Australia)	1.875° × 1.25°
2	ACCESS1.3	CSIRO and BoM (Australia)	1.875° × 1.25°
3	CanESM2	Canadian Centre for Climate Modeling and Analysis (CCCma) of Environment and Climate Change Canada (Canada)	2.8125° × ~2.8125°
4	CMCC-CM	Centro Euro-Mediterraneo sui Cambiamenti Climatici (CMCC) (Italy)	0.75° × 0.7484°
5	CMCC-CMS		1.875° × ~1.9°
6	FGOALS-s2	State Key Laboratory of Numerical Modeling for Atmospheric Sciences and Geophysical Fluid Dynamics, Institute of Atmospheric Physics (LASG/IAP) (China)	2.8125° × 1.6590°
7	INM-CM4.0	Russian Academy of Sciences, Institute of Numerical Mathematics (Russia)	2° × 1.5°
8	IPSL-CM5A-LR	L'Institut Pierre-Simon Laplace (France)	3.75° × ~1.9°
9	IPSL-CM5A-MR	L'Institut Pierre-Simon Laplace (France)	2.5° × ~1.3°
10	IPSL-CM5B-LR	L'Institut Pierre-Simon Laplace (France)	3.75° × ~1.9°
11	MIROC-ESM	Japan Agency for Marine-Earth Science and Technology, Atmosphere and Ocean Research Institute (The University of Tokyo), and National Institute for Environmental Studies (Japan)	~2.8° × ~2.8°
12	MIROC-ESM-CHEM	Japan Agency for Marine-Earth Science and Technology, Atmosphere and Ocean Research Institute (The University of Tokyo), and National Institute for Environmental Studies (Japan)	~2.8° × ~2.8°
13	MPI-ESM-LR	Max Planck Institute for Meteorology (MPI-M) (Germany)	1.875° × ~1.9°
14	MPI-ESM-MR	MPI-M (Germany)	1.875° × ~1.9°
15	MRI-CGCM3	Meteorological Research Institute (Japan)	1.125° × ~1.1°
16	GISS-E2-H	NASA Goddard Institute for Space Studies (GISS) (United States)	2.5° × 2°
17	GISS-E2-R	NASA Goddard Institute for Space Studies (United States)	2.5° × 2°
18	HadGEM2-AO	National Institute of Meteorological Research/Korea Met. Administration (NIMR-KMA) (Korea)	1.875° × 1.25°
19	NorESM1-M	Norwegian Climate Centre (Norway)	2.5° × ~1.9°

Table A2 Comparison of the simulations for 18-h and 6-h spin-up times

Spin-up time	*T*			RH			WS		
	R	BIAS/°C	RMSE/°C	*R*	BIAS/%	RMSE/%	*R*	BIAS/(m·s^{-1})	RMSE/(m·s^{-1})
18-h	0.68	0	1.3	0.7	0.05	4.9	0.4	2.5	2.8
6-h	0.87	0.08	1.27	0.76	−2.7	6.8	0.35	1.9	2.1

Notes: *T* – surface air temperature, RH – relative humidity, WS – windspeed, *R* – correlation coefficient, BIAS – bias, RMSE – root mean square error.

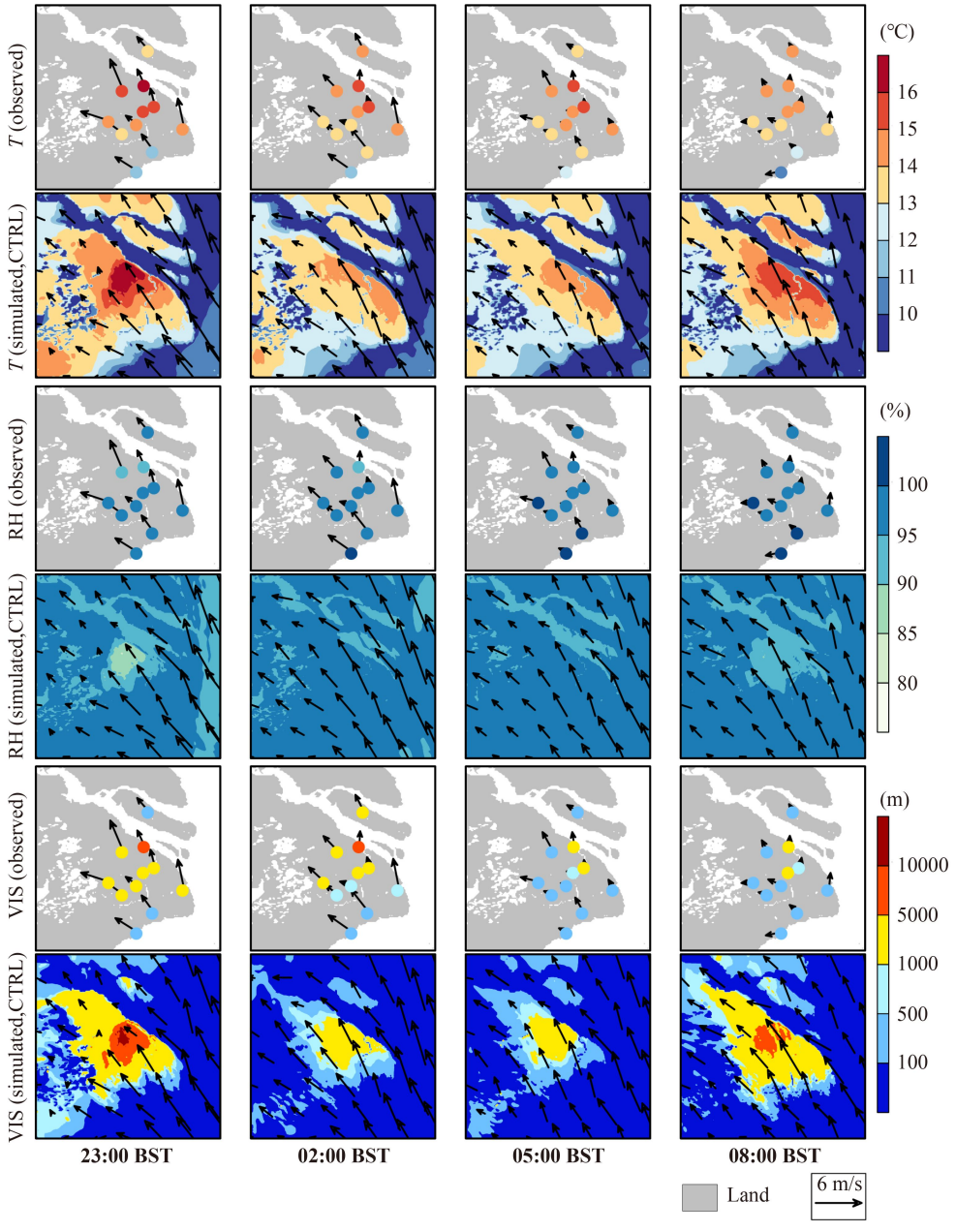

Fig. A2 Spatial distribution of the observed and simulated surface air temperature (*T*), relative humidity (RH) at 2 m, surface visibility (VIS), and wind during the study period. The simulated results are from the control experiment (CTRL). Windspeed magnitude is shown at the bottom right. The gray areas in the figures in the first, third, and fifth rows from the top represent land in the model.

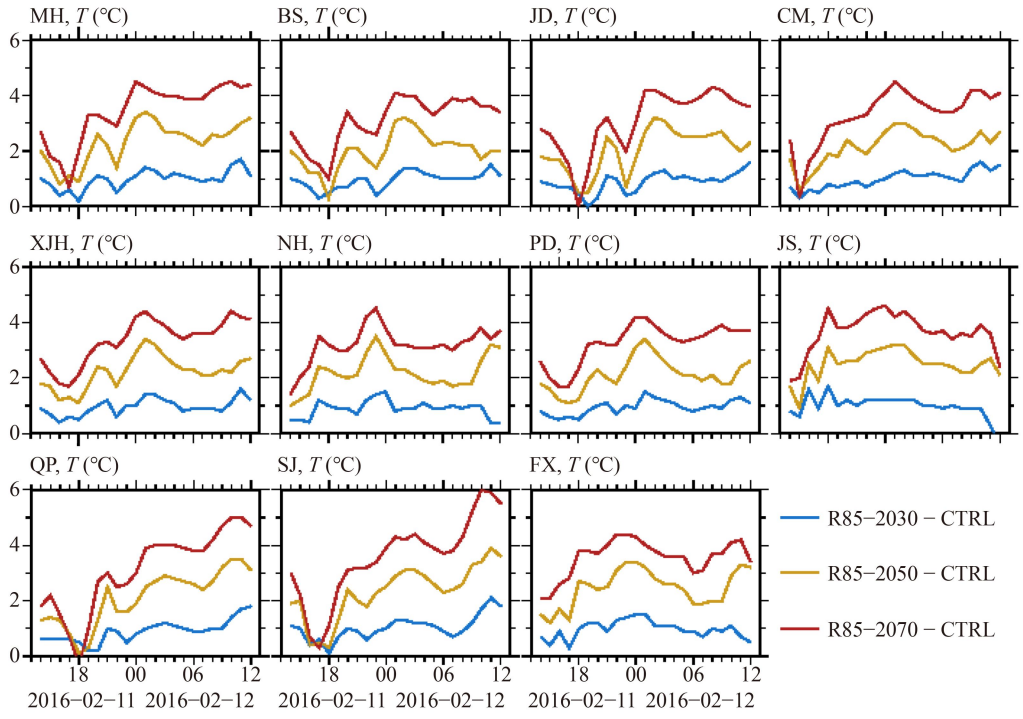

Fig. A3 Time series of surface air temperature (*T*) increase (°C) over that of the control experiment (CTRL) at each station for the three future periods from 2030–2089.

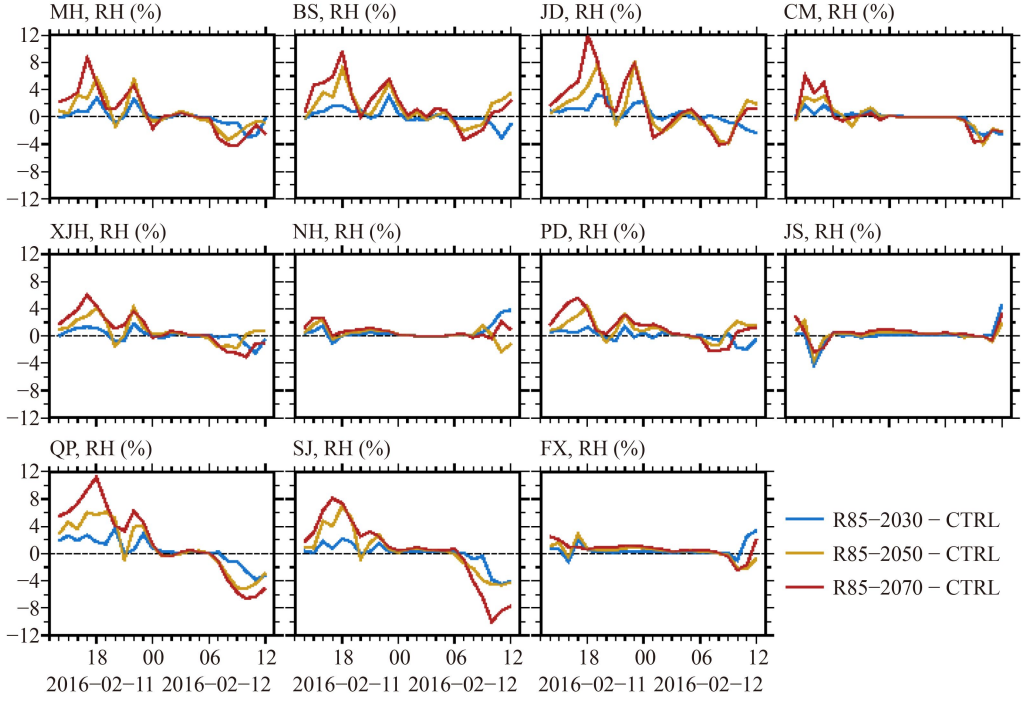

Fig. A4 Same as Fig. A3, but for the change of relative humidity (RH, %) at 2 m. CTRL – control experiment.

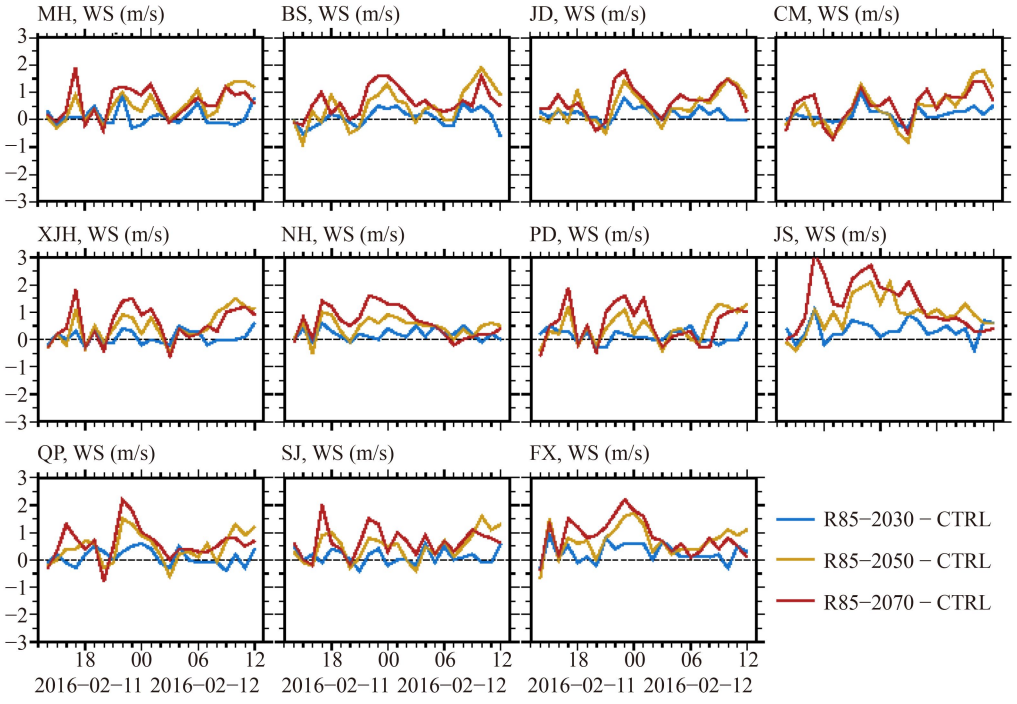

Fig. A5 Same as Fig. A3, but for the change of windspeed (WS; m/s) at 10 m. CTRL – control.

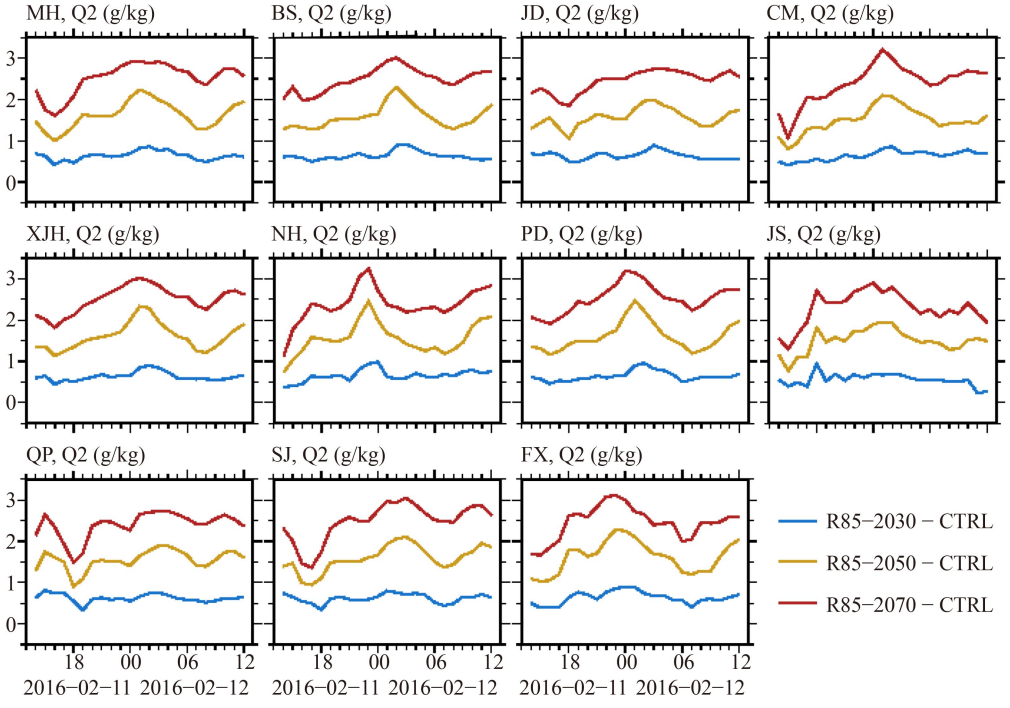

Fig. A6 Same as Fig. A3, but for the change in the water–vapor mixing ratio (g/kg) at 2 m. CTRL – control.

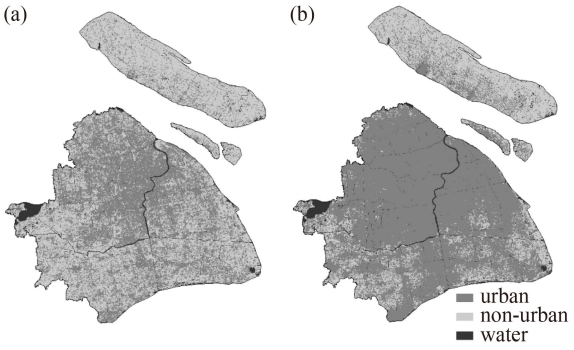

Fig. A7 Distribution of urban and non-urban areas in Shanghai in (a) 2013 and (b) 2030.

References

Belorid M, Lee C B, Kim J C, Cheon T H (2015). Distribution and long-term trends in various fog types over South Korea. Theor Appl Climatol, 122(3–4): 699–710

Byrne M P, O'Gorman P A (2016). Understanding decreases in land relative humidity with global warming: conceptual model and GCM simulations. J Clim, 29(24): 9045–9061

Chen J, Wang Z, Tam C Y, Lau N C, Lau D D, Mok H Y (2020). Impacts of climate change on tropical cyclones and induced storm surges in the Pearl River Delta region using pseudo-global-warming method. Sci Rep, 10(1): 1965–1974

Dai A, Rasmussen R M, Liu C, Ikeda K, Prein A F (2020). A new mechanism for warm-season precipitation response to global warming based on convection-permitting simulations. Clim Dyn, 55(1–2): 343–368

Doan Q V, Kusaka H (2018). Projections of urban climate in the 2050s in a fast-growing city in southeast Asia: the Greater Ho Chi Minh City Metropolitan area, Vietnam. Int J Climatol, 38(11): 4155–4171

Doran J A, Roohr P J, Beberwyk D J, Brooks G R, Gayno G A, Williams R T, Lewis J M, Lefevre R J (1999). The MM5 at the Air Force Weather Agency-New products to support military operations. In: The 8th Conference on Aviation, Range, and Aerospace Meteorology, NOAA/NWS, Dallas, Texas

Gong H, Simwanda M, Murayama Y (2017). An internet-based GIS platform providing data for visualization and spatial analysis of urbanization in major Asian and African cities. ISPRS Int J Geo-inf, 6(8): 257

Gu Y, Kusaka H, Doan V Q, Tan J (2019). Impacts of urban expansion on fog types in Shanghai, China: numerical experiments by WRF model. Atmos Res, 220: 57–74

Kawase H, Yoshikane T, Hara M, Ailikun B, Kimura F, Yasunari T (2008). Downscaling of the climatic changes in the Mei-yu rainband in East Asia by a pseudo climate simulation method. Sci Online Lett Atmos, 4: 73–76

Kawase H, Yoshikane T, Hara M, Kimura F, Yasunari T, Ailikun B, Ueda H, Inoue T (2009). Intermodel variability of future changes in the baiu rainband estimated by the pseudo global warming downscaling method. J Geophys Res, 114(D24): D24110

Kimura F, Kitoh A (2007). Downscaling by pseudo global warming method. The Final Report of ICCAP: 43–46

Kusaka H, Hara M, Takane Y (2012). Urban climate projection by the WRF model at 3-km horizontal grid increment: dynamical downscaling and predicting heat stress in the 2070's August for Tokyo, Osaka, and Nagoya metropolies. J Meteor Soc Japan, 90B: 47–63

Kusaka H, Kimura F (2004). Thermal effects of urban canyon structure on the nocturnal heat island: numerical experiment using a mesoscale model coupled with an urban canopy model. J Appl Meteorol, 43(12): 1899–1910

Kusaka H, Kondo H, Kikegawa Y, Kimura F (2001). A simple single-layer urban canopy model for atmospheric models: comparison with multi-layer and slab models. Boundary-Layer Meteorol, 101(3): 329–358

Lin C, Zhang Z, Pu Z, Wang F (2017). Numerical simulations of an advection fog event over Shanghai Pudong International Airport with the WRF model. J Meteorol Res, 31: 874–889

Liu A, Wang H, Cui Y, Shen L, Yin Y, Wu Z, Guo S, Shi S, Chen K, Zhu B, Wang J, Kong X (2020). Characteristics of aerosol during a severe haze-fog episode in the Yangtze River Delta: particle size distribution, chemical composition and optical properties. Atmosphere (Basel), 11(1): 56–66

Liu W, Han Y, Li J, Tian X, Liu Y (2018). Factors affecting relative humidity and its relationship with the long-term variation of fog-haze events in the Yangtze River Delta. Atmos Environ, 193: 242–250

Niu F, Li Z, Li C, Lee K H, Wang M (2010). Increase of wintertime fog in China: potential impacts of weakening of the Eastern Asian monsoon circulation and increasing aerosol loading. J Geophys Res, 115: D00K20

Niu Z, Wang L, Fang L, Li J, Yao R (2020). Spatiotemporal variations in monthly relative humidity in China based on observations and CMIP5 models. Int J Climatol, 40(15): 6382–6395

Riahi K, Rao S, Krey V, Cho C, Chirkov V, Fischer G, Kindermann G, Nakicenovic N, Rafaj P (2011). RCP 8.5-A scenario of comparatively high greenhouse gas emissions. Clim Change, 109(1–2): 33–57

Sato T, Kimura F, Kitoh A (2007). Projection of global warming onto regional precipitation over Mongolia using a regional climate model. J Hydrol (Amst), 333(1): 144–154

Syed F S, Körnich H, Tjernström M (2012). On the fog variability over south Asia. Clim Dyn, 39(12): 2993–3005

Takemi T, Nomura S, Oku Y, Ishikawa H (2012). A regional-scale evaluation of changes in environmental stability for summertime afternoon precipitation under global warming from super-high-resolution GCM simulations: a study for the case in the Kanto Plain. J Meteorol Soc, 90A(SI): 189–212

Taniguchi K, Sho K (2015). Application of the pseudo global warming dynamic downscaling method to the Tokai heavy rain in 2000. J Meteor Soc Japan Ser. II, 93(5): 551–570

Taylor K E, Stouffer R J, Meehl G A (2012). An overview of CMIP5 and the experiment design. Bull Am Meteorol Soc, 93(4): 485–498

van Vuuren D P, Edmonds J, Kainuma M, Riahi K, Thomson A, Hibbard K, Hurtt G C, Kram T, Krey V, Lamarque J F, Masui T, Meinshausen M, Nakicenovic N, Smith S J, Rose S K (2011). The representative concentration pathways: an overview. Clim Change,

109(1–2): 5–31

Willett K M, Dunn R J H, Thorne P W, Bell S, de Podesta M, Parker D E, Jones P D, Williams C N Jr (2014). HadISDH land surface multi-variable humidity and temperature record for climate monitoring. Clim Past, 10(6): 1983–2006

Williams A P, Schwartz R E, Iacobellis S, Seager R, Cook B I, Still C J, Husak G, Michaelsen J (2015). Urbanization causes increased cloud base height and decreased fog in coastal Southern California. Geophys Res Lett, 42(5): 1527–1536

Wu J, Zha J, Zhao D, Yang Q (2018). Changes in terrestrial near-surface wind speed and their possible causes: an overview. Clim Dyn, 51(5–6): 2039–2078

Xu Z F, Yang Z L (2017). Relative impacts of increased greenhouse gas concentrations and land cover change on the surface climate in arid and semi-arid regions of China. Clim Change, 144(3): 491–503

Xu Z, Han Y, Yang Z (2019). Dynamical downscaling of regional climate: a review of methods and limitations. Sci China Earth Sci, 62(2): 365–375

Zeng Z, Ziegler A D, Searchinger T, Yang L, Chen A, Ju K, Piao S, Li L Z X, Ciais P, Chen D, Liu J, Azorin-Molina C, Chappell A, Medvigy D, Wood E F (2019). A reversal in global terrestrial stilling and its implications for wind energy production. Nat Clim Chang, 9(12): 979–985

Zhou S, Zheng J (1987). Shanghai urban influence of fog. Acta Meteorol Sin, 45: 366–369 (in Chinese)

AUTHOR BIOGRAPHIES

Ying Gu has a B.Sc. in Geographical Science in 2004 and Ph.D. Sc. in physical geography in 2010 from East China Normal University, Shanghai, China. She is a lecturer at Shanghai University of Engineering Science, Shanghai, China. Her research focuses on urban atmospheric environment and numerical analyzing and modeling. She has published 10 peer-reviewed articles related to fog, anthropogenic heat, air pollution, data assimilation. E-mail: guying@sues.edu.cn.

Hiroyuki Kusaka has a Ph.D. in Science in 2002 from University of Tsukuba, Japan. He is a Professor at University of Tsukuba and studies urban climate and local winds. He is best known worldwide for designing the WRF model's first urban canopy scheme. He has published over 120 peer-reviewed articles in urban climatology, mountain meteorology, and applied meteorology. Prof. Kusaka is the recipient of the Helmut E. Landsberg Award 2021 of the American Meteorological Society (AMS).

Quang-Van Doan has Ph.D. in science from the University of Tsukuba, Japan, in 2016. He is working as an assistant professor at the Center for Computational Sciences, the University of Tsukuba since 2019. He is known as an expert in urban climatology with a focus on the impacts of urbanization on urban heat island and rainfall processes, statistical and numerical modeling. He has published over 30 peer-reviewed articles on urban climate, urban canopy modeling, machine learning, applied meteorology. Prof. Quang-Van Doan is a member of multiple professional societies, such as the Meteorological Society of Japan, the American Meteorological Society, the American Geophysical Union, Asia Oceania Geosciences Society. He is currently serving on the Board on Urban Environment of the American Meteorological Society. E-mail: Doanvan.gb@u.Tsukuba.ac.jp.